PHYSICAL REVIEW D

PARTICLES AND FIELDS

THIRD SERIES, VOLUME 28, NUMBER 1 1 JULY 1983

Polarization and magnetic moment of the Σ^- hyperon

L. Deck,* A. Beretvas, T. Devlin, K. B. Luk, R. Rameika,† and R. Whitman‡
Physics Department, Rutgers—The State University, P.O. Box 849, Piscataway, New Jersey 08854

R. Handler, B. Lundberg, L. Pondrom, M. Sheaff, and C. Wilkinson
Physics Department, University of Wisconsin, Madison, Wisconsin 53706

P. T. Cox,§ C. Dukes, J. Dworkin, and O. E. Overseth
Department of Physics, University of Michigan, Ann Arbor, Michigan 48109

K. Heller
Physics Department, The University of Minnesota, Minneapolis, Minnesota 55455

(Received 17 January 1983)

We have measured the magnetic moment of the Σ^- hyperon to be $\mu(\Sigma^-)=-0.89\pm0.14$ nuclear magnetons. The magnitude of the polarization of Σ^- produced at 7.5 mrad by 400-GeV protons in the process $p+\mathrm{Be}\rightarrow\Sigma^-+X$ averages $(15.5\pm3.6)\%$ over the momentum range 120 to 290 GeV/c. The mean Σ^- transverse momentum was 1.32 GeV/c. The polarization direction at production is the same as Σ^+ and opposite that of Λ and Ξ^0.

I. INTRODUCTION

Since the discovery that Λ hyperons produced by protons at high energy are polarized,[1] a number of experiments have been performed to explore that effect further for Λ's and other hyperons,[2–7] and to use the polarization to measure hyperon magnetic moments.[8–10] These experiments have stimulated much theoretical work to understand the polarization mechanism,[6,11,12] and to refine models of baryon structure in the light of the new, precise magnetic-moment data.[13–28]

The experiment reported here yielded a final sample of 516 229 $\Sigma^-\rightarrow n\pi^-$ events collected in the M2 hyperon beam at Fermilab. A statistically significant polarization signal was observed. This provided high-statistics data on the Σ^- magnetic moment through a measurement of precession of the polarization vector in a magnetic field. The previously reported attempt, based on about 28 000 Σ^- produced in a low-energy exclusive final state, yielded -0.71 ± 1.25 nuclear magnetons.[29] More precise results were obtained from two experiments which studied the fine structure in x rays from Σ^- atoms.[30,31] In both experiments, two opposite-sign values of the moment fit the data. Choosing the negative solutions, the weighted average of all previous experiments is -1.41 ± 0.25 nuclear magnetons. Early results of an improved measurement of the fine-structure splitting in Σ^- lead have been reported by Roberts,[32] and recent preliminary results from an experiment similar to the one described here have been reported by Marriner.[33]

A number of difficulties which hindered earlier precession measurements were overcome in this experiment. First, the precision of the method improves directly with the magnitude of $\int B\,dL$ along the path of the Σ^-. Polarized Σ^- available from low-energy exclusive reactions typically travel only a fraction of a meter before decay. In this experiment, the mean decay length was about 7 m and all Σ^- in our sample passed through 5.95 T m of magnetic field. Second, the precision is limited by the small decay asymmetry ($\alpha\approx7\%$) for $\Sigma^-\rightarrow n^-$. With a polarization of about 15%, this yields a 1% effect to be measured in the decay angular distributions. A large sample of Σ^- was needed to reduce statistical uncertainties. Finally, systematic errors were controlled by having two samples of Σ^- which had opposite polarization, but which were nearly identical in all other respects.

In the following sections, we will discuss the apparatus and data-collection procedures, the reconstruction of $\Sigma^-\rightarrow n\pi^-$ events, the analysis of the decay distributions to determine the polarization vector, and the determination of the magnetic moment. Finally, we will compare these results with similar measurements of other hyperons and with a simple quark model of baryon structure.

II. APPARATUS AND DATA-COLLECTION PROCEDURES

A. General remarks

The basic recipe used here to measure the Σ^- magnetic moment has three ingredients. The Σ^-'s must be produced with a polarization vector which either is known or can be determined. They must pass through a known magnetic field in which the coupling between the magnetic moment and the field causes their spins to precess. The polarization vector must be measured after they emerge from the field. The experimental apparatus described in this section is designed to accomplish these objectives. Additional details can be found in Ref. 34.

B. Production of Σ^-

The experiment was performed in the M2 beam in the Meson Laboratory at Fermilab. Protons at 400 GeV were transported from the synchrotron to the primary Meson Laboratory target at typical intensities of order 3×10^{12} protons per machine pulse (ppp). The steering was arranged so that the M2 beam line accepted 400-GeV protons diffractively scattered from the Be target at about 0.7 mrad. This angle was varied as needed to maintain the intensity in the M2 line at $\sim5\times10^8$ ppp.

The first stage of the beam-transport system consisted of a string of dipole magnets and a quadrupole doublet which brought the secondary beam to an intermediate focus 201 m from the main Meson Laboratory target. A similar system produced a final focus on the hyperon production target at 450 m from the Meson Laboratory target. The beam was instrumented with segmented-wire ion chambers (SWIC's) at both foci. The spot size at the hyperon target was 3mm vertical by 4 mm horizontal [full width at half maximum (FWHM)].

With an unpolarized beam and target, parity conservation in strong interactions allows polarization only for particles produced at nonzero angles relative to the incoming proton momentum. The polarization must be in the direction perpendicular to the production plane, i.e., on the axis defined in Fig. 1 by $\hat{k}_{\rm in}\times\hat{k}_{\rm out}$ where $\hat{k}_{\rm in}$ is the direction of the incident proton momentum and $\hat{k}_{\rm out}$ is the direction of the outgoing hyperon momentum. The polarization is zero for production directly forward, and its direction reverses if the production angle is reversed. Figure 1 also shows the target coordinate system, the first of two used to describe this experiment.

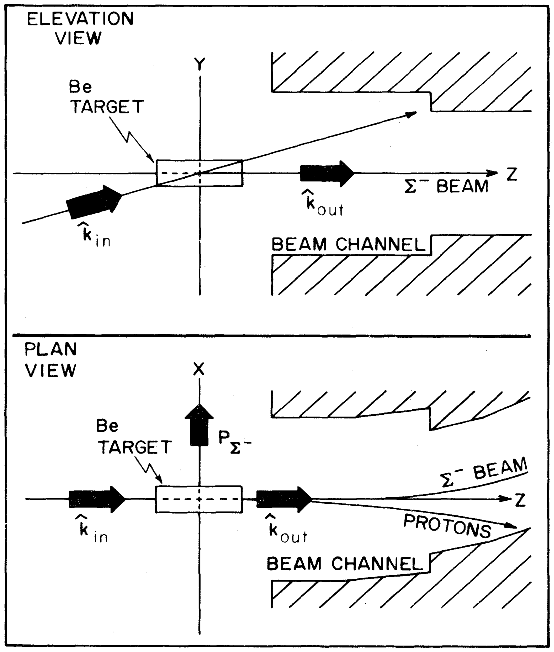

FIG. 1. The target coordinate system is defined at the production target located at the entrance to the beam channel. The Z axis points downstream, tangent to the central channel orbit. The Y axis is vertically upward, and the X axis (horizontal) completes a right-handed coordinate system. The directions of both the incident proton momentum $\hat{k}_{\rm in}$ and the outgoing Σ^- momentum $\hat{k}_{\rm out}$ are in the Y-Z plane. The parity-allowed direction for the Σ^- polarization is along the X axis. The case shown, with the proton beam aimed upward, is defined as a positive production angle.

The hyperon beam channel and detection apparatus (described below) were kept in fixed positions for the duration of this experiment. Variation of the production angle was accomplished by moving the proton beam with a vertical steering system. This consisted of a magnet located at 335 m from the primary target which deflected the protons above or below the horizontal median plane, and a string of three magnets ($M1$ in Fig. 2) at 442 m which restored the beam to the median plane at the position of the hyperon-production target. For this experiment, the steering system was operated at production angles of $+7.5$ and -7.5 mrad in the Y-Z plane.

In the vertical view, there was a slight shift in the position and angular distribution of the negative beam when the production angle was reversed, caused by slight differences in alignment and the variation of the production cross section with angle. This is discussed in Secs. III E and III F. The horizontal position and angular distribution of the beam did not change when the production angle was reversed.

The production target was a Be rod, 0.635 cm in diameter by 15.3 cm long. A remotely controlled target manipulator permitted operation with the target out of the beam for background studies. In addition to the SWIC, the target area was instrumented with an argon-filled ion chamber to monitor the proton beam intensity. A set of scintillation counters was inserted for beam tuning and ion-chamber calibration and was removed during data collection. A schematic diagram of the target area is shown in Fig. 3.

C. The beam channel

The beam channel consisted of a 5.3-m-long magnet, with a pole-tip spacing of 3.81 cm. For these measurements, it was operated at a field integral of 5.95 ± 0.01 T m, measured from the center of the production target through the downstream fringe field. The field was set

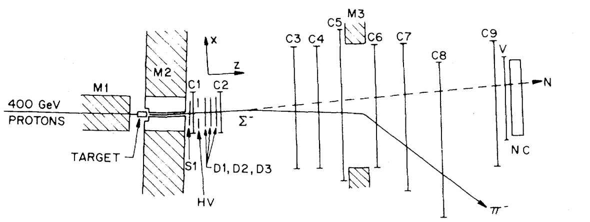

FIG. 2. A plan view of the M2 charged-hyperon apparatus as configured to detect $\Sigma^-\to n\pi^-$. Magnet $M1$ was used to vary the angle in the vertical plane at which the proton beam struck the Σ^- production target. $M2$ served to define the Σ^- beam and precessed the Σ^- spin vector in the X-Z plane. A conventional wire-chamber spectrometer array $C1$–$C8$, $D1$–$D3$, and $M3$ determined the trajectories of the Σ^- and π^- downstream of $M2$. $C9$ was physically present, but not used in this experiment. An array of scintillator, lead, and steel (NC) was used to signal the presence of the neutron in the event.

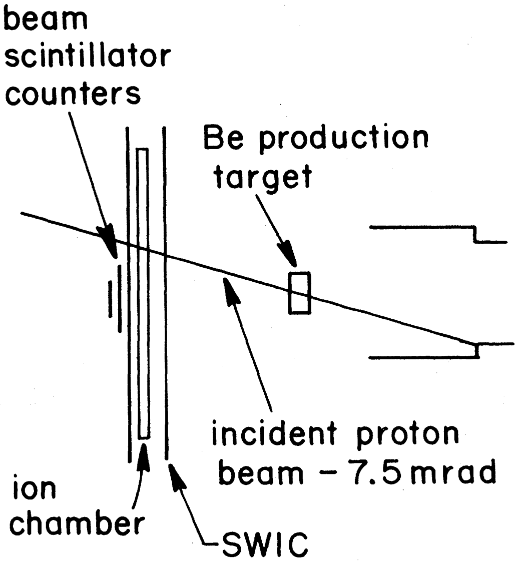

FIG. 3. A schematic representation of the hyperon-production target, associated detectors, and entrance to the beam channel. The scintillation counters were removed during data collection. The longitudinal scale is compressed relative to the transverse scale.

and monitored by a proton-resonance probe in a standard position against which the field integral was calibrated. Run-to-run fluctuations in the field integral were at most 0.1%. The channel served several purposes: to define a negatively charged beam and eliminate neutral and positively charged particles, to act as a spectrometer for measuring the Σ^- momentum, and to precess the polarization vector of the beam.

The channel consisted of a series of brass blocks, typically 60 cm long, with straight, cylindrical holes approximately centered on the central orbit (Fig. 4). Defining apertures made of tungsten were placed halfway through the magnet (4 mm diameter) and at the exit (10 mm diameter). The central orbit through the magnet had a bend angle of 10 mrad. The acceptance was 1.2 μsr at the central orbit momentum of 177 GeV/c. The relative acceptance for stable charged particles as a function of momentum was determined by Monte Carlo simulation of the channel and is shown in Fig. 5. The coordinate system at the target is defined in Figs. 1 and 4. The Z axis remains everywhere tangent to the central orbit.

The production target and the limiting aperture of the channel placed strong constraints on the trajectories through the beam channel. The horizontal position and direction of a particle emerging from the channel were each strongly dependent on its momentum. To the extent that the target and aperture are pointlike, the momentum can be determined exactly from either the position or direction. We define

$$\rho = P_t(1/P - 1/P_0) , \tag{2.1}$$

where P_t is the bending power of the magnet in GeV/c, and P is the momentum of a particle. P_0 is the central orbit momentum, i.e., the momentum of a particle which originates at the center of the target, passes through the center of the limiting aperture in the channel, and bends exactly 10 mrad. By definition, the central orbit emerges exactly on the Z axis of the downstream coordinate system. Assuming pointlike target and aperture, the horizontal position and direction of a particle at the channel exit are

$$X = L_2\rho/2 , \tag{2.2}$$

$$dX/dZ = \rho(L_1 + 2L_2)/2L , \tag{2.3}$$

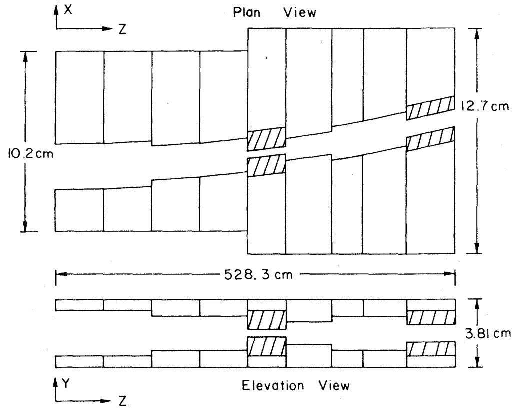

FIG. 4. Plan (X-Z) and elevation (Y-Z) views of the central core of the charged-hyperon beam channel. The piecewise straight cylindrical holes through brass are approximately centered on a circular orbit with a total bend of 10 mrad. The cross-hatched regions represent tungsten inserts which form the limiting aperture and the exit aperture. Note the different longitudinal and transverse scales.

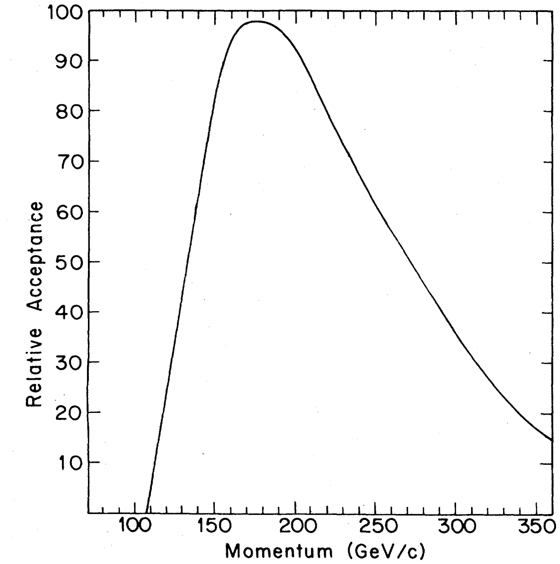

FIG. 5. The relative momentum acceptance for stable charged particles of the charged-hyperon beam channel with the field integral set at 5.95 T m. An acceptance of 100 corresponds to the full solid angle of the limiting channel aperture for a point source. The finite size of the target decreases the acceptance slightly for the central momentum.

where L_1, L_2, and $L = L_1 + L_2$ are defined in Fig. 6. Clearly, there is a virtual image upstream of the channel exit at a distance

$$L_N = X/(dX/dZ) = LL_2/(L_1 + 2L_2) \ . \tag{2.4}$$

Thus, the two constraints can be restated as a single constraint that the particle originate at this virtual image, plus a relationship between the momentum and angle at the channel exit [Eq. (2.3].

The finite sizes of the production target and the limiting aperture can be converted into an uncertainty in the virtual image size (1.5 mm standard deviation) and an uncertainty (typically 8%, dominated by target size) for the momentum determined from the exit angle. This information was used in the geometric and kinematic fits discussed in Sec. III.

D. The spectrometer

The spectrometer (Fig. 2) was designed to detect and permit reconstruction of the decay $\Sigma^- \rightarrow n\pi^-$. The production target and the central tungsten aperture of the channel defined two points on the Σ^- orbit in $M2$, and a set of multiwire proportional chambers (MWPC's) and drift chambers (DC's) gave data on the charged-particle trajectories through the rest of the system. The characteristics of the chambers are listed in Table I. The drift chambers are described in more detail in Ref. 35. The orbit through $M2$ was used to determine the Σ^- momentum, and the orbit through $M3$ was used to determine the π^- momentum. A hadron calorimeter was used to detect the presence of the neutron from the decay.

The upstream detectors ($C1$, $C2$, $D1$—D_3) were used to measure the Σ^- trajectory after $M2$. The trajectory determined the Σ^- momentum through Eqs. (2.3) and (2.4). For some events the decay vertex occurred within this array. (See Sec. III B.) However, most events decayed in an evacuated pipe 8.5 m long by 36 cm in diameter immediately downstream of these chambers.

The pion trajectory before and after $M3$ was defined by $C3$—$C8$. $C9$ was used to detect long-lived beam tracks and for calibration studies. Helium-filled polyethylene bags were placed in the regions between most of these chambers to reduce multiple scattering and interactions in air.

The analyzing magnet $M3$ had superconducting coils and an iron yoke with an aperture 20.3 cm high by 61 cm wide. The pole tips were 183 cm long. Typically, its field integral was 3.17 T m, and it was determined by two independent methods: a field map and analysis of charged tracks. Aberrations up to sextupole components were determined and corrected in the event reconstruction.

Several plastic scintillation counters were used. $S1$ was a 10-cm-diameter counter at the exit of $M2$. HV was 10 cm by 30 cm with a 5-cm-by-3.8-cm hole which served to veto beam halo. V was used to veto charged particles entering the hadron calorimeter.

The neutron counter was an array of plastic scintillators, lead, lead-glass, and steel as shown in Fig. 7. It was designed strictly as a neutral-hadron trigger, and it could not absorb the entire energy of most neutron showers. The signal NC used in the trigger consisted of at least one minimum-ionizing particle in any of the last three scintillators.

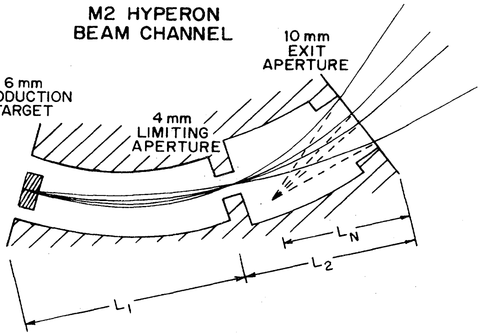

FIG. 6. A schematic representation of the beam-channel virtual image which combines the constraints of the production target and limiting aperture for trajectories through the M2 channel. The transverse dimensions and the bend angle have been greatly exaggerated for clarity of presentation.

The pulse heights from all scintillators in the neutron counter were recorded and used to check the stability of the results against variation of the pulse-height threshold.

E. Calibration and performance

The wire chambers were positioned perpendicular to the Z axis, with horizontal wires level within 1 mrad. This was checked with charged tracks. The Z positions were measured to ± 0.3 cm. The wire spacing for each chamber was accurately determined during construction.

The position of the Z axis through each chamber was established with the proton beam. This was done by tuning $M2$ to transport 400-GeV protons at very low intensity on the central orbit of the beam channel, and turning off $M3$. Events were selected in which there was one and only one hit in each plane with a good fit to a straight line in each view using approximate values for the center wires. The centroid of the wire hit distribution in each plane defined the values of the center wire used in the analysis. The process was refined by computing the difference between the predicted and actual chamber hit positions for large samples of fitted tracks. The precision of this process for locating the Z axis is better than ± 0.1 mm.

Drift chambers were calibrated cell by cell by using tracks already fitted to MWPC information. Figure 8 shows a plot of the drift time as a function of the position of the tracks in a cell. The slope and vertex of the V-shaped fit to the data yielded the desired calibration constants. The spatial resolution of the DC data for these linear calibration constants varied between 0.22 and 0.27 mm for the various planes. Because the negative beam was concentrated in one or two cells of each drift-chamber plane, it was necessary to keep the singles rates less than 200 000 per machine spill in order to maintain the DC efficiency at 80% or above. This upstream singles rate corresponded to approximately 50 000 tracks through the full spectrometer.

The steering of the proton beam onto the production target fluctuated slightly with time, as did the field in $M3$. Therefore, it was necessary to determine from the data the

TABLE I. Wire-chamber characteristics.

Chamber		Number of wires	Cell size (mm)	Resolution (mm)	Typical efficiency (%)	Z position (cm)
DC1	X	3	20.4	0.22	81	107.6 113.0
	Y	3	30.4	0.22	60	96.6 102.1
DC2	X	7	20.4	0.27	83	276.1 281.8
	Y	5	30.4	0.27	76	287.7 293.3
DC3	X	11	20.4	0.24	84	452.9 458.4
	Y	7	61.0	0.24	85	464.0 469.5
C1	X	24	2	0.57	96.2	68.4
	Y	32	2	0.57	96.1	67.4
C2	X	128	2	0.57	98.8	506.8
	Y	128	2	0.57	97.1	505.8
C3	X	256	2	0.57	99.6	1318.6
	Y	128	2	0.57	99.3	1317.6
C4	U	128	2	0.57	96.9	1603.8
	V	128	2	0.57	96.9	1602.8
C5	X	256	2	0.57	99.9	1857.8
	Y	152	2	0.57	99.9	1855.9
C6	X	256	2	0.57	99.8	2254.5
	Y	128	2	0.57	99.6	2253.5
C7	X	640	2	0.57	100.0	2586.4
	Y	192	2	0.57	99.8	2585.4
C8	X	640	2	0.57	93.6	3031.1
	Y	192	2	0.57	88.7	3026.6

effective target position and $M3$ field integral for each data tape. Samples of "beam pions" (tracks which did not decay—mostly π^-) and kinematically reconstructed Σ^-'s were used to do this in the following way. The value of the field integral for $M2$, which was measured and monitored with a proton-resonance probe, was assumed to be correct. The beam pions were used to determine the variation of the effective target and defining aperture positions as functions of an assumed value for the $M3$ field integral. Consistent sets of these parameters were then used to reconstruct $\Sigma^- \rightarrow n\pi^-$ events. The set which gave the

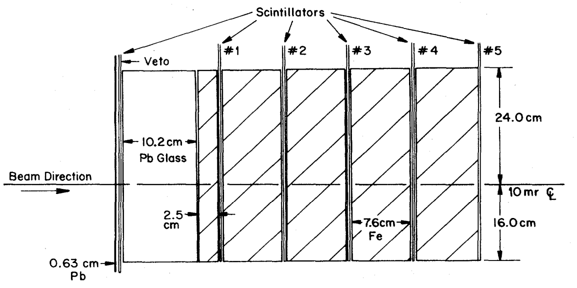

FIG. 7. A plan view of the final configuration of the neutron counter. The vertical height of NC was 20 cm, centered on the beam line. Changes from an earlier configuration are discussed in the text.

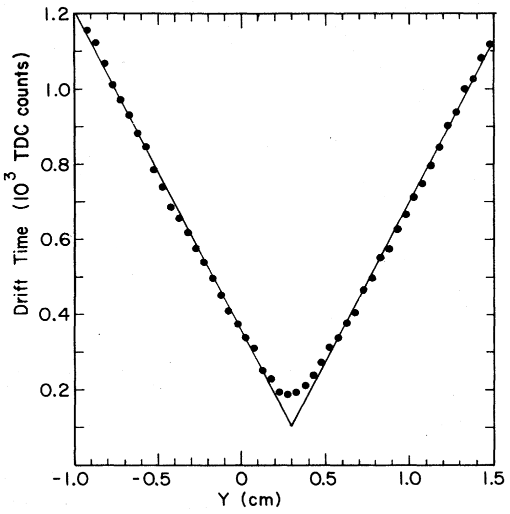

FIG. 8. Drift-chamber calibration. Tracks were binned (0.5-mm bins) according to where they intersected the cell under calibration based on MWPC data. A histogram of the drift time for events in each bin showed a sharp peak. This figure shows a plot of the drift time at this peak as a function of the mean position of the tracks in the bin. The slope and vertex of the V-shaped fit to the data yield the desired calibration constants.

correct Σ^- mass was chosen for use in the reconstruction program. This method gave values for the $M3$ field integral completely consistent with those determined from its current and excitation curve.

For momenta higher and lower than the central channel momentum, parts of the target were obscured by the channel apertures. This was used to refine the Σ^- momentum calculation by making a first-order correction in the effective horizontal target position.

F. The trigger

The fast-electronic-logic system used prompt pulses from the MWPC's and from scintillation counters to trigger the data acquisition process. The system was configured to detect a charged particle emerging from $M2$, with both a neutral hadron and a negatively charged particle downstream of $M3$, as a signature for $\Sigma^- \rightarrow n\pi^-$.

A pulse from $S1$ was used to provide a sharp timing signal from a charged particle entering the detector from the beam channel. HV was used to veto charged particles in the halo around the negative beam. $C3$ completed the signature for a charged track upstream of $M3$. This signal

$$S = S1 \cdot \overline{\mathrm{HV}} \cdot C3$$

was then put in coincidence with the right half of chamber 7, $C7R$, to ensure that the charged particle was negative. A veto counter V in front of the neutron calorimeter ensured that the signal from NC came from a neutral particle. The Σ^- trigger was

$$\Sigma^- = S \cdot C7R \cdot \bar{V} \cdot \mathrm{NC}\ .$$

This signal was used to trigger the readout procedure. Also, the coincidence $S \cdot V$, prescaled by a factor of 512, was allowed to act as a trigger to provide a sample of beam tracks for various calibrations. Typically, there were about 150 Σ^- triggers and 50 prescaled $S \cdot V$ triggers per 0.8-sec beam spill for 5×10^8 incident protons.

G. Data-acquisition system

A CAMAC/PDP-11 system was used to read the data, record it on magnetic tape and to check system performance. Upon detection of an event trigger, a "busy" logic level was set to prevent further triggers, and the digitization process was started, i.e., gated flip flops (latches) for the MWPC's and various counter signals, time-to-digital converters for the drift chambers, and analog-to-digital converters for the neutron calorimeter pulse height. An interrupt signal to the computer began the read sequence which started with the MWPC's and latched data and then proceeded to the slower analog-to-digital converters (ADC's) and time-to-digital converters (TDC's). Upon completion of this process, all registers were reset and the busy level removed in preparation for another event.

A set of twelve 2048-byte buffers was used to store the data temporarily in the computer memory. Each typically held about ten events and, when filled, was placed in a queue to be copied to temporary storage on a high-speed disk. After copying took place the buffer was available for new events. Between synchrotron spills, the data were recorded on 800 BPI magnetic tape.

At the end of each spill, a set of scalers which monitored various counting rates was read into the computer, flagged appropriately, and stored in sequence in an event buffer. These data included readings from an ion chamber in the proton beam which struck the hyperon production target, total charged-track rate in the negative beam, and single-count rates in proportional chambers as well as the standard event trigger. Some channels were devoted to ungated rates not subject to the busy condition so that dead-time effects could be monitored.

Also between spills, any data remaining in the buffers in computer memory was used for on-line computation which checked the system performance. No event reconstruction was attempted at this level.

The typical dead time for reading one event was about 1 msec. The data rate was maintained between 100 and 200 events per spill because of the charged-track rate in the drift chambers. (See Sec. II E.) Thus, the dead time was about 15%.

III. EVENT RECONSTRUCTION

In order to extract the polarization and magnetic moment of the Σ^- from the raw data, a number of tasks were necessary. First, the events with the geometric properties of $\Sigma^- \rightarrow n\pi^-$ were identified and separated from background events. The single most important topological property in the pattern recognition was the detection of the decay vertex, i.e., the presence of a kink in a single charged track. Second, kinematic fitting identified Σ^- events and eliminated further backgrounds. Third, the acceptance of the detector and the integrity of the analysis programs were tested by processing a sample of Monte Carlo events with known properties. Fourth, various properties of the experimental apparatus were determined and stability monitored from the data itself. This section describes this part of the analysis. We reserve for Sec. IV a discussion of the asymmetry in the decay angular distribution of the neutron momentum vector which gave the polarization vector from which the physically interesting information is derived. Figure 9 is a flow chart which shows the main features of the analysis programs.

At all stages of the analysis, comparisons were made amongst data taken at different times, at different production angles, and between real data and Monte Carlo events.

A. The real data sets

Data were taken in two separate time periods of less than one week each. The only significant change in the apparatus between the two sets was restructuring and realignment of the neutron detector to make it more efficient and to center it more closely on the observed beam distribution. The neutron detector was moved vertically about 1 cm to center it better on the beam, and a section was added to increase its thickness by 7.6 cm of iron. Table II shows the principal characteristics of the two data sets (labeled A and B). They were analyzed by the same programs, but kept separate because of somewhat different geometric properties of the neutron detector. Final results were combined as discussed in Sec. IV.

Yields for the full data set B are shown in Table III. The true production angles differed slightly from the nominal values, and this caused a difference in the yield of

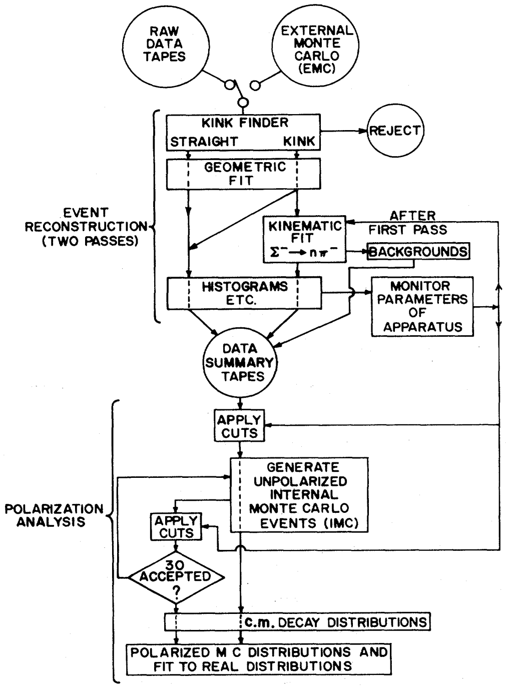

FIG. 9. A flow chart of the data-analysis programs. Details are discussed in the text.

Σ^- per incident proton. If we assume that the cross section varies as $e^{-3P_t^2}$, then the observed differences are consistent. It also caused a slight difference in the magnitudes of the polarization vectors at the two angles. The final polarization will be the average of the two magnitudes. The precession angle is independent of the magnitude and will not be affected.

An important feature of the data set is the existence of equal amounts of data at opposite production angles. The data were taken in matched sets of tapes at the two angles with as little variation in conditions as possible. Comparison of the decay asymmetries between these two samples is essential in bias elimination because the Σ^- polarization reverses, while apparatus biases do not. This is discussed fully in Sec. IV.

B. The Monte Carlo data sets

A distinction must be made between the external Monte Carlo (EMC) calculations and the internal Monte Carlo (IMC) calculations. In order to check the properties of the pattern recognition programs and to study backgrounds, the EMC was written to generate samples of events with properties as close as possible to the real sample and to propagate them through a computer-simulated version of the detection apparatus. Appendix A describes this more fully. Over 1 000 000 such events were put through the full analysis programs to test for reconstruction efficiency, computer-induced biases, and to check the ability of the analysis programs to detect known polarization and biases in a sample of events.

The IMC is a hybrid Monte Carlo technique discussed more fully in Appendix B and in Ref. 36. It was used primarily in the polarization analysis (Sec. IV). The distinction is made here to avoid confusion.

C. Pattern recognition and geometric reconstruction

A search for a topological pattern of hits in the MWPC's was the first step in the data analysis. A hit is defined for the MWPC data as the position of one isolated wire or the average position of two adjacent wires. For the drift chambers a hit was defined as the position determined from a single cell.

In the Y-Z projection, the procedure required one and only one hit for at least two chambers in the set $C3$, $C5$, $C6$, $C7$, and $C8$. If this requirement was satisfied, it further required that at least one more hit be added from the

TABLE II. The data sets.

	A	B
Total tapes	22	30
Tapes at +7.5 mrad	11	15
Tapes at −7.5 mrad	11	15
Reconstructed $\Sigma^- \rightarrow n\pi^-$	108 377	407 852
Typical values		
Events/tape	50 000	95 000
Multiparticle hadronic events (unreconstructible)	25 000	50 000
Straight tracks	15 000	25 000
Kinked tracks	10 000	21 000
Various cuts[a]	5 100	6 700
Reconstructed Σ^- which satisfy all cuts	4 900	13 600
Running time/tape	1.5 h	2 h

[a] Loose cuts on χ^2, Σ^-, and π^- momenta, and the decay-vertex position were made in selecting raw events to be written on data-summary tapes. These were tightened and others added in two additional stages of cuts. Summed through all three stages the fractions of events cut were distributed as follows: Σ^- and π^- momenta, 24%; various χ^2 cuts, 29%; decay-vertex position, 39%; various apertures, 8%. This pattern is strongly dependent on the order in which the cuts were applied. Most of the events discarded in the last two cuts were good Σ^-.

TABLE III. Counting statistics and yields on the data set B.

	-7.5	$+7.5$
Nominal production angle (mrad)	-7.5	$+7.5$
True production angle (mrad)	-7.7 ± 0.1	$+7.0 \pm 0.1$
Average P_t (GeV/c)	1.350 ± 0.018	1.227 ± 0.018
Protons on target	1.3×10^{12}	0.8×10^{12}
Σ^- triggers	1.15×10^{6}	1.23×10^{6}
Reconstructed Σ^-	1.94×10^{5}	2.14×10^{5}
Σ^-(reconstructed)/Σ^-(triggers)	0.168	0.174
Σ^-(reconstructed)/proton	1.49×10^{-7}	2.68×10^{-7}
Σ^-/proton (observed ratio)	0.56	
Σ^-/proton (expected ratio assuming $e^{-3P_t^2}$ dependence)	0.39 ± 0.12	

remaining chambers in the same set.

In the X-Z projection, the program used all combinations of hits in chambers $C3$, $C4$, and $C5$, two at a time, to form a track segment upstream of magnet $M3$. At least two hits in chambers $C6$, $C7$, and $C8$ were required to form a downstream track segment which intersected the upstream track at the bend vertex in $M3$.

These minimum requirements could be met by either a straight beam track, of the daughter pion from a Σ^- which decayed upstream of $C4$. Whenever they were satisfied, the program added as many hits as possible from the remaining MWPC's and drift chambers.

All events which reached this stage of the pattern recognition were written to data summary tapes, even though subsequent stages of the event analysis program flagged them as rejects.

The position of the kink, or decay vertex, was located by assuming it to be in each possible interval between successive wire chambers, i.e., $C1$-$D1$, $D1$-$D2$,...,$C4$-$C5$. A fit (geometric χ^2) to the full track was performed which found the best Z position for a vertex in each interval. This fit assumed a common vertex for both views and a bend in the horizontal plane at $M3$. It also used the production target and collimator in the Y-Z plane and the beam-channel virtual image (see Sec. II C) in the X-Z plane as constraints. The hypothesis with the best χ^2 was kept for subsequent analysis. Typically, there were about 25 data points and eight parameters, yielding 17 degrees of freedom for these fits. The geometric χ^2 distribution is shown in Fig. 10.

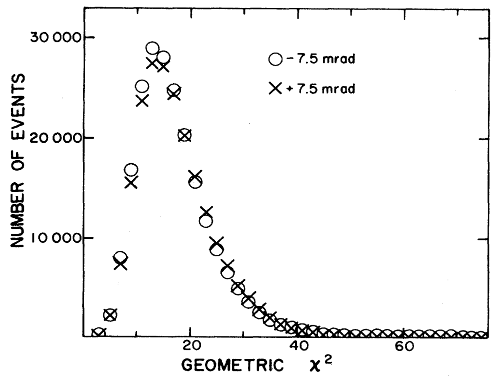

FIG. 10. The geometric χ^2 distribution for events which satisfied all other cuts. Events with χ^2 above 55 were cut. The -7.5 mrad data have been renormalized to the same area as the $+7.5$ mrad data.

Every track was then subjected to a "no-kink" hypothesis, i.e., a χ^2 fit was made under the assumption that all hits in both views upstream of $M3$ fell on a single straight line in space. This removes three degrees of freedom in the fit. Any event for which χ^2 increased by less than 7.0 was assumed to be a straight track. This implies a cut on small decay angles in the lab system. In fact, the EMC established that less than 1% of the Σ^- events were lost by this cut, and the opening angle distributions of the real and EMC events agreed quite well (Fig. 11).

Events with geometric χ^2 greater than 55 were cut. The EMC established that less than 1.4% of the Σ^- events were lost by this cut, and the principal reason was π^- decay in flight.

The Σ^- track, i.e., that portion of the track upstream of the decay vertex, was required to have at least three drift-chamber hits (category 1) or two drift-chamber hits (category 2) per view. This ensured the minimum information needed to perform momentum analysis on the Σ^-

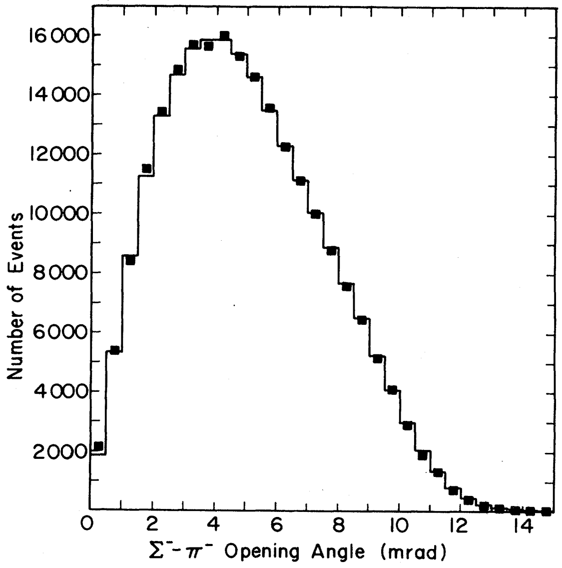

FIG. 11. The distribution of angles between the Σ^- and π^- tracks. The squares represent real data and the lines represent external Monte Carlo events. Contamination by nondecaying beam tracks should populate the bin from zero to 1 mrad. The difference between the real and Monte Carlo data is consistent with 0.1% contamination from this source, and it is the same at both production angles. No cut was made on this variable.

trajectory through magnet $M2$. Although the two categories were ultimately combined, studies of mass and momentum resolution and comparisons with EMC were done separately to monitor quality. Both categories imply vertex cuts, since the decay must reach the appropriate chamber before the conditions are satisfied. Category 2 does not imply inferior quality, but merely early decay.

Σ^- events generated by the EMC showed the programs to be 98% efficient for decay vertices downstream of 600 cm. Figure 12 shows the dependence on Z position, and also demonstrates that the major reason for the drop to 72% efficiency upstream of 600 cm was inefficiency in the drift chambers.

D. Momentum determination and further cuts

Before a full kinematic fit was attempted, the momenta of the track segments through $M2$ and $M3$ were computed, and several cuts were made on the events.

The momentum vector for the Σ^- was determined from the best fit to the measured track in the chambers and the target and collimator constraints as discussed in Sec. II C. The Σ^- momentum spectrum is shown in Fig. 13.

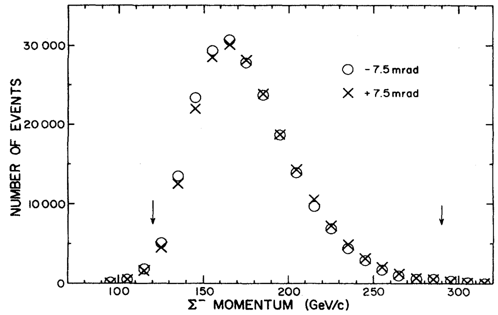

FIG. 13. The momentum distribution for Σ^- with all other cuts applied. The arrows indicate the momentum cuts at 120 and 290 GeV/c. The -7.5 mrad data have been renormalized to the same area as the $+7.5$ mrad data.

The channel acceptance was completely negligible below 105 GeV/c, and small below 120 GeV/c. Events with Σ^- momenta below the latter value were cut from the data sample. The EMC showed that a nondecaying track through the beam channel and the spectrometer could reconstruct as a kink because of measurement errors. In such cases the momentum of the "daughter pion" was the beam momentum, always greater than 105 GeV/c, with a reconstructed "parent Σ^-" momentum above 292 GeV/c. To eliminate such misidentified events, Σ^- with momenta above 290 GeV/c were cut.

The π^- momentum was determined from the wire-chamber data downstream of the decay vertex and the field integral of $M3$. The uncertainty in this is less than 1%. The momentum spectrum for daughter pions is shown in Fig. 14. With the cuts on Σ^- momentum stated above, the maximum momentum for a daughter pion is 93.5 GeV/c. Therefore, events in which the track through $M3$ had momenta greater than 95 GeV/c were cut. Because of the channel acceptance, this eliminated scattered pions which originated in the production target.

Another property of EMC straight tracks which reconstructed as kinked tracks is the distribution of "kink positions" which is shown in Fig. 15. They cluster in positions where the wire-chamber data cannot constrain them. Events with kink positions upstream of 170 cm or downstream of 1800 cm in Z were cut. The corresponding distribution for real Σ^- events is shown in Fig. 16. If the EMC calculation is accurate, 96% of any straight-track background is eliminated by this cut. Real Σ^- eliminated

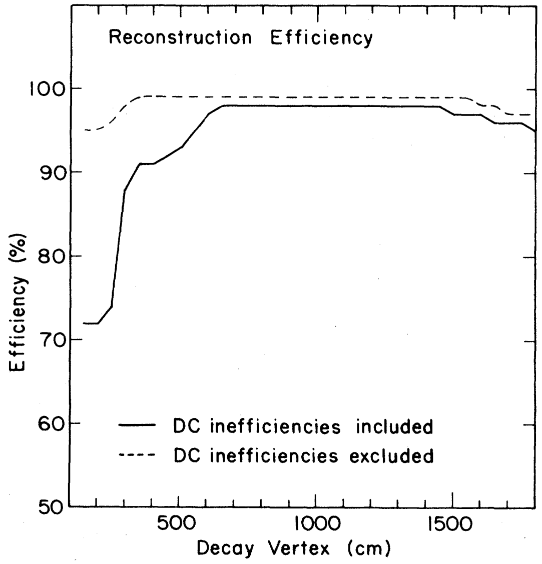

FIG. 12. The reconstruction efficiency for Monte Carlo–generated $\Sigma^- \rightarrow n\pi^-$ events as a function of the Z position of the decay vertex. This was done with and without the drift-chamber inefficiencies imposed on the Monte Carlo calculation. Note the suppressed zero on the vertical scale.

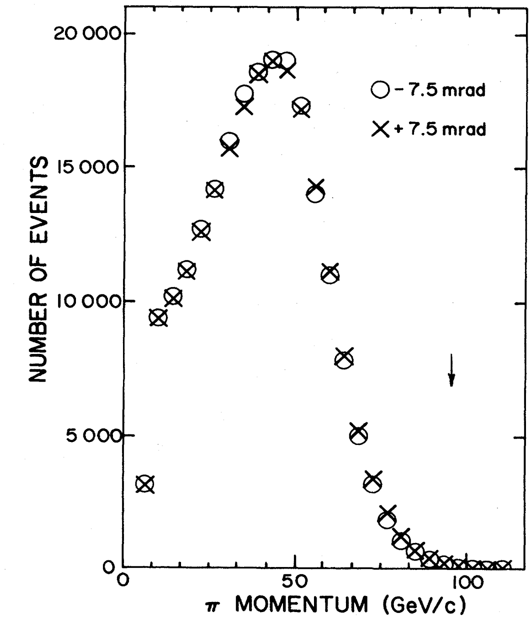

FIG. 14. The momentum distribution for pions from $\Sigma^- \rightarrow n\pi^-$. All cuts have been made except for the 95-GeV/c cut on this variable. The -7.5 mrad data have been renormalized to the same area as the $+7.5$ mrad data.

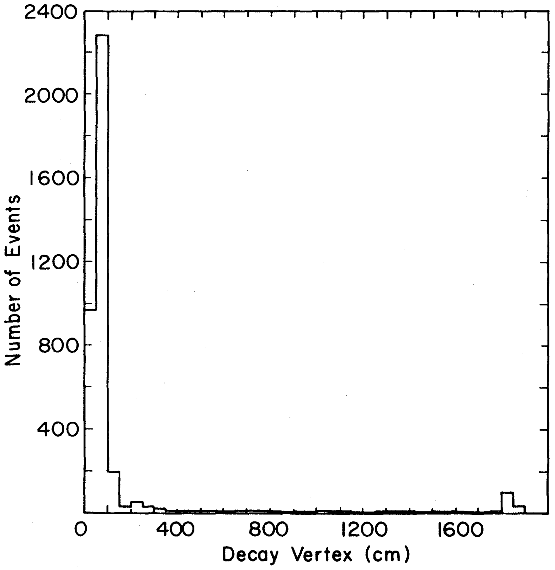

FIG. 15. The "decay-vertex" distribution for straight tracks generated by the external Monte Carlo program and reconstructed as kinked tracks. For most such events the reconstruction program cannot form a "kink" with reasonable χ^2 anywhere except at the ends of the region covered by the wire chambers.

by this cut tend to have either the Σ^- or the π^- track poorly determined relative to the bulk of the events.

E. Kinematic reconstruction

Events which passed the above cuts were subjected to the full kinematic reconstruction. This was done entirely from the charged-track information, since the NC was strictly a trigger requirement and provided no precise information about the neutron momentum vector. The kinematic fit used the raw chamber data and was identical to the geometric fit, except that the hypothesis $\Sigma^- \rightarrow n\pi^-$ was assumed. This added one constraint: the Σ^- mass, 1.197 35 GeV/c^2. The change in χ^2, i.e., the kinematic χ^2

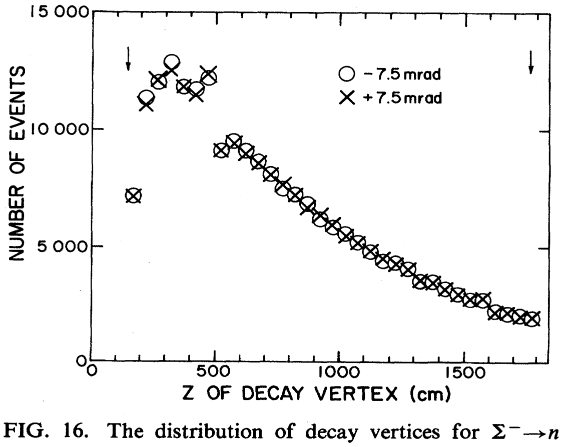

FIG. 16. The distribution of decay vertices for $\Sigma^- \rightarrow n\pi^-$ events which have satisfied all cuts. The cuts in this variable (arrows) strongly suppress background from straight tracks. Compare with Fig. 15. The -7.5 mrad data have been renormalized to the same area as the $+7.5$ mrad data.

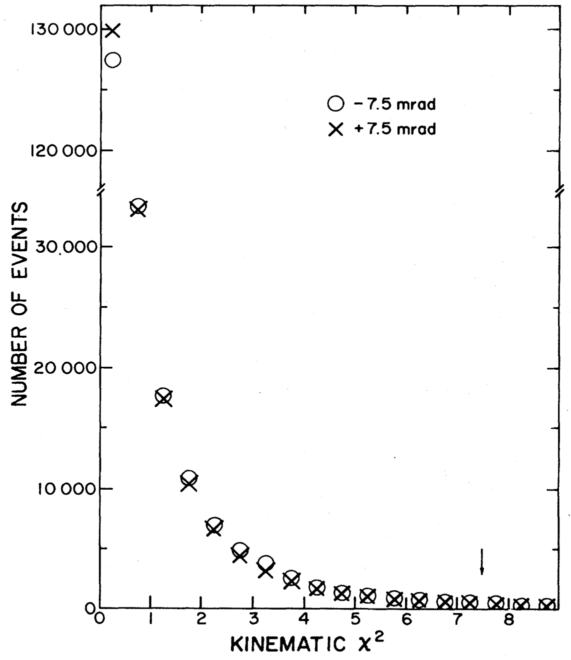

FIG. 17. The distribution of kinematic χ^2 for events in which all other cuts are satisfied. This is the increase in χ^2 over the geometric χ^2 when the fit was repeated with the additional constraint of the Σ^- mass. Events with an increase in χ^2 greater than 7.5 (arrow) were eliminated. The -7.5 mrad data have been renormalized to the same area as the $+7.5$ mrad data.

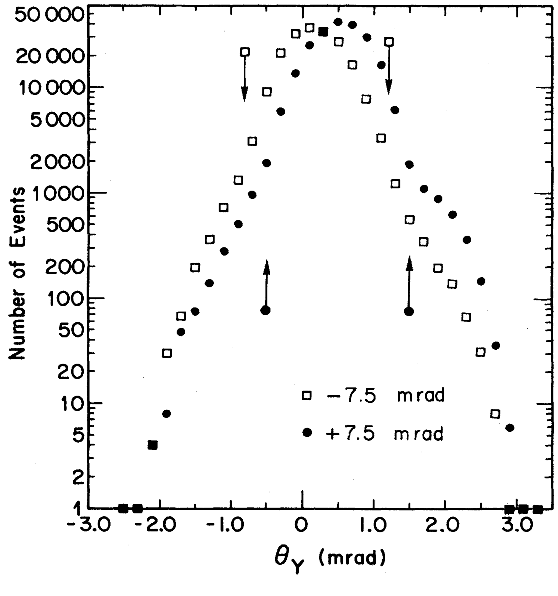

FIG. 18. The distribution of angles θ_Y for the Σ^- momentum projected on the vertical (Y-Z) plane for events which satisfy all other cuts. The distribution shifted slightly when the production angle was reversed. Production from sources other than the target is small and largely obscured by the tails of the main peak. Some evidence for a shoulder near $+2$ mrad can be seen in the $+7.5$ mrad data. Events further than 2.7 standard deviations from the centroids of the distributions (arrows) were cut.

is shown in Fig. 17. Events with a change in χ^2 greater than 7.5 were cut from the sample. This cut eliminated 4.6% of those events which survived all other cuts.

F. Backgrounds

A number of possible sources were studied to identify contributions to any residual background in the sample of kinematically reconstructed Σ^-.

A number of "target out" tapes were written to study other sources of Σ^- production. The rate was small, about 0.5% that of the "target in" rate. About two-thirds of this can be explained by production from air in the vicinity of the target. The remainder was probably produced in the SWIC and ion chamber (IC) (Fig. 3), and in the beam channel. Evidence for production in the SWIC and IC can be seen in Fig. 18, which shows histograms for θ_Y. The shoulder in one of the distributions is at the 0.4% level.

Although the SWIC and IC were perfectly legitimate sources for Σ^-'s, a cut was made at ± 2.7 standard deviations about the central peak in θ_Y. This eliminated 1.5% of the Σ^-'s in the final sample and made negligible changes in the final results for the polarization and magnetic moment, but it greatly improved the agreement between real and Monte Carlo distributions.

Two topologically similar decay processes were investigated as sources of backgrounds: $K^- \rightarrow \pi^- \pi^0$ and $\Xi^- \rightarrow \Lambda\pi^-$ with the subsequent neutral decay of the Λ. Both can fulfill the trigger requirements and provide a kink-track topology. The acceptance of the spectrometer for both processes is good.[34] To study the contribution from these processes, a missing-mass calculation was performed on every Σ^- event using the charged tracks to compute the mass of the missing neutral under each hypothesis.

Figure 19 shows the missing-mass distribution for the Ξ^- hypothesis before and after cuts. The Ξ^- contamination in the uncut sample is estimated to be 2.5%. EMC calculations demonstrated that the cuts removed 90% of the Ξ^- events. Therefore, the Ξ^- contamination in the final sample is estimated to be 0.25%. Figure 20 shows the corresponding curve for the K^- hypothesis. No clear evidence of K^- contamination can be seen. For comparison, a sample of EMC-generated K^- events is shown, normalized to a contamination level of 0.5%. This would represent a three-standard-deviation contribution to the real curve. The cuts rejected 90% of the K^- events. Therefore, this source of contamination is estimated to be less than 0.05%. Independent estimates of the contamination level, based on cross sections, decay rates, and detection probabilities, are consistent with these numbers.

Possible contamination by nondecaying beam tracks misidentified as kinked tracks was discussed in Sec. III B. Cuts on the Z position of the kink suppressed such events (Fig. 15), and the opening-angle distribution (Fig. 11) shows such contamination is not more than 0.1%.

Another cut was considered to study the possibility of events in which γ rays triggered the neutron counter instead of neutrons. Figure 21 shows the pulse-height spectrum for counters 3, 4, and 5. Since there were 14.4 radiation lengths of lead, lead-glass, and steel upstream of counter 3, electromagnetic showers were mostly absorbed before reaching these counters. About 5.2% of the events have pulse heights less than 200 counts, corresponding to an energy deposition of about 5 GeV. No significant change in any of the distributions was observed when events in this region were cut, nor was there any change in the final polarization or magnetic moment at the level of 0.1 standard deviations. Stability of the final answers

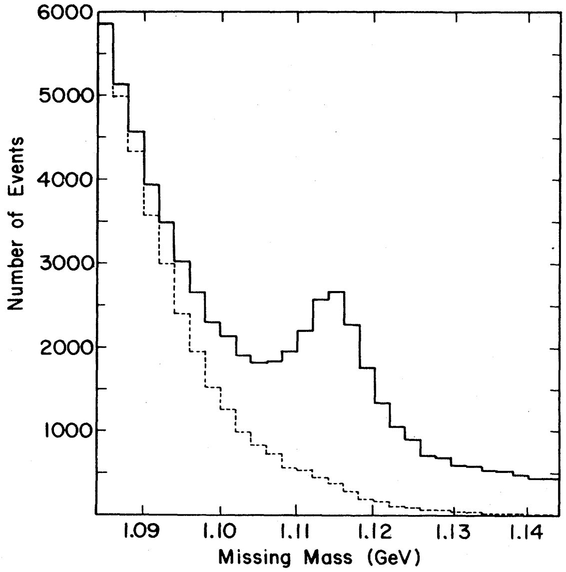

FIG. 19. Missing-mass distribution under the hypothesis that the events are $\Xi^- \rightarrow \Lambda\pi^-$ before (solid line) and after (dashed line) cuts. A clear Λ signal is seen in the uncut sample. The kinematic χ^2 cut was the most effective in removing Ξ^- events. True $\Sigma^- \rightarrow n\pi^-$ events fall into a large peak off scale to the left.

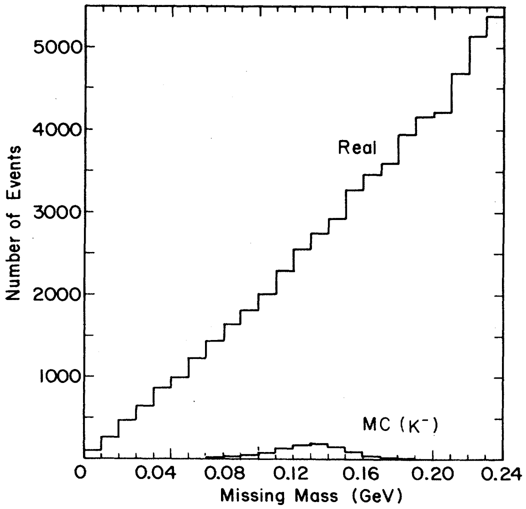

FIG. 20. Missing-mass distribution under the hypothesis that the events are $K^- \rightarrow \pi^- \pi^0$ before cuts. No evidence for a π^0 missing-mass peak is seen. A Monte Carlo–generated sample of K^- events normalized to 0.5% of the real events is shown for comparison. Subsequent cuts reduced the Monte Carlo sample by a factor of 10.

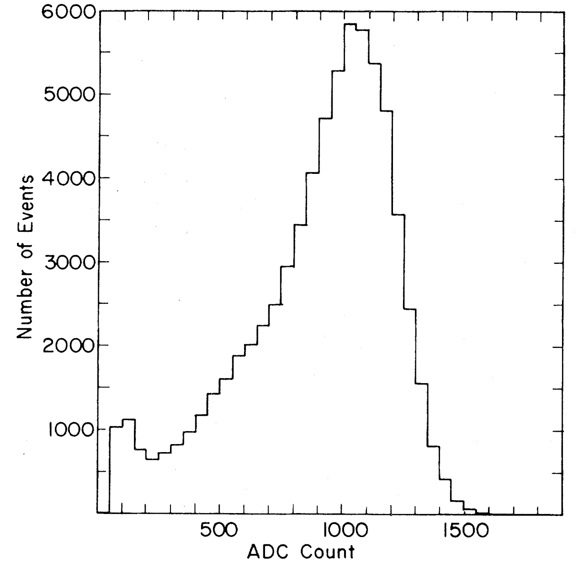

FIG. 21. The distribution of pulse heights, summed over counters 3, 4, and 5 of the neutron counter, for events which satisfy all cuts.

against NC cuts is discussed in detail in Ref. 34. No cut on NC was made in the final data sample.

The total background in the final sample from all sources was estimated by examining a Σ^- mass histogram (Fig. 22) for data in which all cuts except the kinematic χ^2 had been made. The result was 1.8%. Of this, as much as 0.4% could be attributed to the sources discussed above which have negligible effect on the polarization. The remaining 1.4% background must be from unknown sources or Σ^- events which were poorly reconstructed for various reasons.

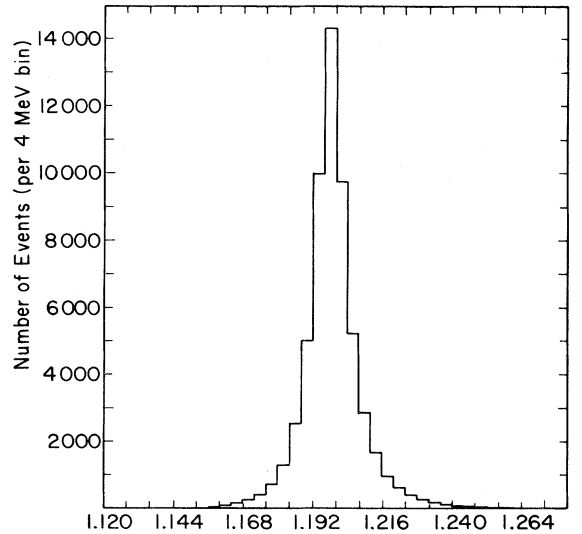

FIG. 22. A histogram of the effective mass of the parent particle Y^- for the decay process $Y^- \rightarrow n\pi^-$. This was computed with the three-momenta of Y^- and π^- before the Σ^- mass constraint was applied in the kinematic χ^2 fit. All cuts have been applied to the events in this histogram except the kinematic χ^2 cut.

The sensitivity of the result to these backgrounds was studied by varying the cut on kinematic χ^2 (equivalent to a mass cut for this one-constraint fit). The magnetic moment varied by less than 0.2 standard deviations for cuts as low as 1.0 and as high as 13.0. The kinematic χ^2 cut chosen for the final event selection was 7.5. See Ref. 34 for more details.

G. Aperture cuts

A number of aperture cuts were applied to both real and Monte Carlo data. Any event which passed outside these boundaries was rejected. The edges of the areas covered by sense wires in all MWPC's were used as apertures. The $-X$ edges of $C7$ and $C8$ were the most important of these. Another cut (0.5 cm in Y and 2.0 cm in X) was made inside the physical opening of the spectrometer magnet $M3$.

The neutron counter was a limiting aperture in the vertical distribution, and it requires some discussion. Approximately equal amounts of data were collected at the two production angles ±7.5 mrad. The fact that the polarization reversed sign when the production angle was reversed, whereas the acceptance of the apparatus remained unchanged, was exploited in the polarization analysis discussed in Sec. IV. Although the apparatus did not change, the angular distribution of the beam did change with production angle (Fig. 18). Thus, the effective acceptance varied because NC was illuminated differently when the angle was reversed.

An example of this is the reconstructed daughter neutron trajectory projected to NC which is shown in Figs. 23

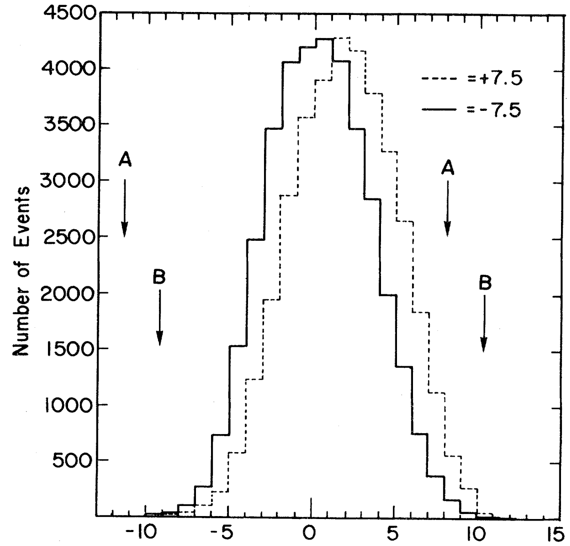

FIG. 23. The distribution of Y positions at which the daughter neutron struck the neutron counter, plotted for the two production angles. The arrows indicate the vertical boundaries of NC for the two data sets. NC was moved after these distributions were plotted for the set A and found to be off center. This is most likely responsible for the Y asymmetry in that data set. The data set B for which NC was approximately centered, showed no Y asymmetry.

and 24. A substantial difference is seen in the Y distributions, whereas the X distributions are virtually identical. Since NC is a limiting aperture, parts of the neutron-decay angular distribution will be lost, and these losses will involve different parts of that distribution when the production angle is reversed.

This can be expected to introduce a spurious signal in the Y component of the polarization if the Monte Carlo simulation of the beam and apparatus is not perfect. Fortunately, the Y component is known to be zero by parity conservation and the fact that any spin precession is in the X-Z plane. The X and Z components are free of this particular pathology.

The effect was studied extensively by applying various aperture cuts inside NC. The final cuts were chosen symmetrically about the centroid of the distribution of neutron trajectories projected to NC. For each angle ±7.5 mrad a cut was placed 1 cm inside the vertical boundary nearest the centroid, and another an equal distance from the centroid on the other side. The effects of this will be discussed in Sec. IV.

IV. POLARIZATION ANALYSIS

A. Method

The polarization of the Σ^- sample was determined from the asymmetry of the neutron distribution in the Σ^- rest system. This distribution can be written

$$dN=(1+\alpha\vec{\mathbf{P}}\cdot\hat{p}_n)d(\cos\theta)/2\ , \qquad (4.1)$$

where $\alpha=-0.068\pm0.008$,[29,37] $\hat{p}_n$ is the unit vector along the neutron momentum in the Σ^- rest frame, $\vec{\mathbf{P}}$ is the Σ^- polarization, and θ is the angle between $\hat{p}_n$ and $\vec{\mathbf{P}}$. The asymmetry was measured with respect to each of the three axes of a right-handed coordinate system with the Z axis parallel to the laboratory Σ^- momentum, the X axis is horizontal, and the Y axis approximately vertical. Within about 2 mrad, this system is parallel to the spectrometer coordinate system. The projected distributions are

$$dN_i=(1+\alpha P_i\cos\theta_i)d(\cos\theta_i)/2\ , \qquad (4.2)$$

where $i=X,Y,Z$.

These equations are true only if the spectrometer acceptance and pattern recognition programs are perfect. A more realistic representation of the distributions for the two production angles ±7.5 mrad is given by

$$dN_{i\pm}=G_{\pm}(\cos\theta_i)(1\pm\alpha P_i\cos\theta_i)d(\cos\theta_i)/2\ , \qquad (4.3)$$

where $G_{i\pm}(\cos\theta_i)$ is the acceptance function. The acceptance changed with production angle, not because the spectrometer changes, but because the Σ^- beam distribution changed slightly (Fig. 18) and sampled its apertures differently. An important task of the polarization analysis program was to determine the acceptance as accurately as possible. The internal Monte Carlo procedure, a hybrid technique described in Appendix B, was used for this purpose. Since all parameters except $\cos\theta$ of each real event are used to generate IMC events, the IMC events sample the apertures of the detector in exactly the same way as the real events.

There still remains the possibility that the properties of the apparatus are not perfectly reproduced by the IMC. Thus the measured asymmetry in Eq. (4.3) includes an ap-

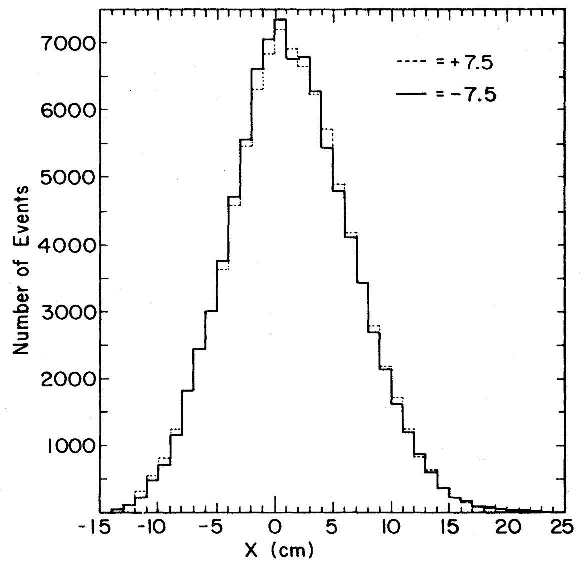

FIG. 24. The distribution of X positions at which the daughter neutron struck the neutron counter, plotted for the two production angles. The horizontal boundaries of NC were at −16 and +24 cm, and were not changed between the two data sets. Note that the distributions are virtually identical for the two production angles.

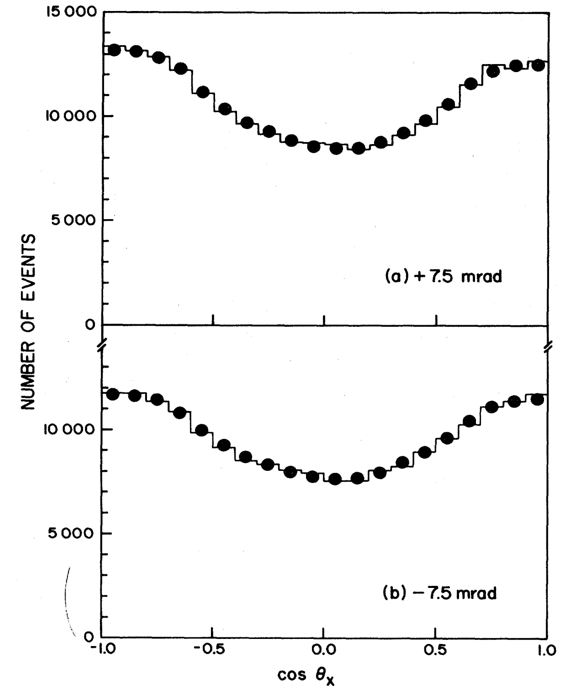

FIG. 25. The $\cos\theta_X$ distribution of neutrons in the Σ^- rest frame for $\Sigma^-\rightarrow n\pi^-$ decay for +7.5 mrad (a) and −7.5 mrad (b). The dots represent the distribution of internal Monte Carlo events which have been "polarized" to produce the best fit to the real data. Since αP_X is small, this curve is approximately the acceptance of the apparatus as a function of $\cos\theta_X$.

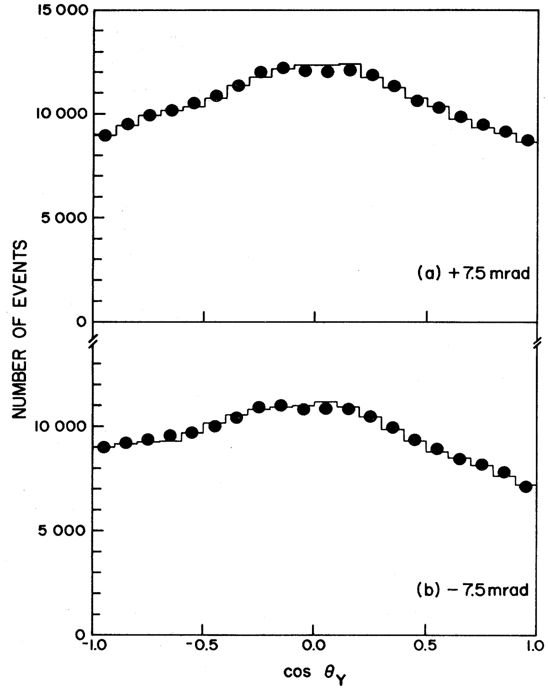

FIG. 26. The $\cos\theta_Y$ distribution of neutrons in the Σ^- rest frame for $\Sigma^-\rightarrow n\pi^-$ decay for + 7.5 mrad (a) and −7.5 mrad (b). The dots represent the distribution of internal Monte Carlo events which have been "polarized" to produce the best fit to the real data. Since αP_Y is small, this curve is approximately the acceptance of the apparatus as a function of $\cos\theta_Y$. Note the significant difference in shapes for (a) and (b).

paratus bias, and we must replace αP_i by

$$A_{i\pm}=\pm\alpha P_i+B_i\ , \tag{4.4}$$

where $A_{i\pm}$ are the experimentally measured asymmetries, and B_i are any remaining biases of the apparatus not corrected by the IMC. The sign of the polarization reverses when the production angle reverses, but the apparatus bias remains the same. The latter is a necessary assumption in this analysis.

Once the values of $A_{i\pm}$ have been obtained, the sums and differences yield the polarization and biases.

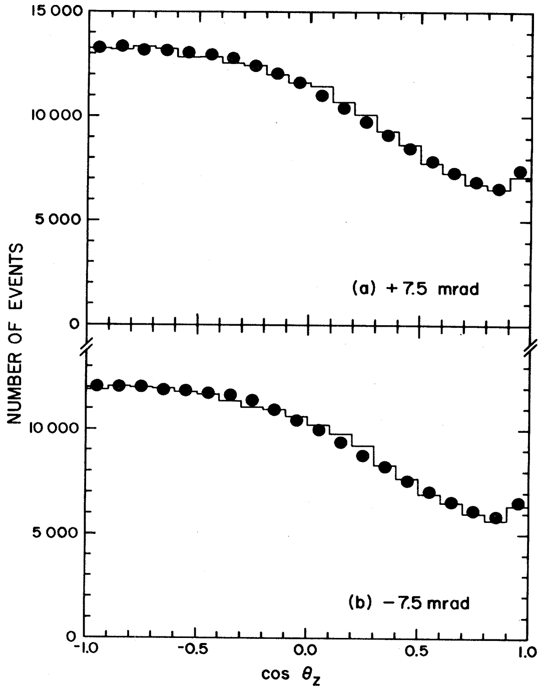

FIG. 27. The $\cos\theta_Z$ distribution of neutrons in the Σ^- rest frame for $\Sigma^-\rightarrow n\pi^-$ decay for + 7.5 mrad (a) and −7.5 mrad (b). The dots represent the distribution of internal Monte Carlo events which have been polarized to produce the best fit to the real data. Since αP_Z is small, this curve is approximately the acceptance of the apparatus as a function of $\cos\theta_Z$.

B. The neutron angular distributions

Figures 25—27 show the angular distributions in the Σ^- rest system of the daughter neutrons from $\Sigma^-\rightarrow n\pi^-$ with respect to each of the three coordinate axes and for the two production angles. Also shown are the IMC distributions which have been "polarized" to produce the best fit to the real data.

Table IV shows the results for P_i and B_i the two pattern-recognition categories of events and the two data-collection periods defined in Sec. III A. Although the

TABLE IV. Polarization signals and biases: pattern categories.

Data set	Category (Sec. III B)	αP_X	X Bias
B	1	-0.0098 ± 0.0029	-0.0279 ± 0.0029
B	2	-0.0112 ± 0.0058	$+0.0298\pm0.0058$
A	1	-0.0114 ± 0.0055	$+0.0512\pm0.0055$
		αP_Y	Y bias
B	1	$+0.0014\pm0.0032$	-0.0506 ± 0.0032
B	2	-0.0021 ± 0.0070	-0.0301 ± 0.0070
A	1	-0.0128 ± 0.0061	-0.0880 ± 0.0070
		αP_Z	Z bias
B	1	$+0.0010\pm0.0034$	-0.0480 ± 0.0034
B	2	$+0.0064\pm0.0081$	-0.0631 ± 0.0081
A	1	$+0.0019\pm0.0066$	-0.0680 ± 0.0066

TABLE V. Polarization signals and biases: high- and low-momentum samples.

Data set	Bin (GeV/c)	$\langle P \rangle$ (GeV/c)	$\langle P_t \rangle$ (GeV/c)	$\langle X_F \rangle$	αP_X	X bias
B	$P<175$	154	1.16	0.38	-0.0092 ± 0.0034	-0.0171 ± 0.0034
B	$P>175$	202	1.52	0.50	-0.0112 ± 0.0038	-0.0159 ± 0.0039
B	All	176	1.32	0.44	-0.0100 ± 0.0025	-0.0166 ± 0.0025
A	All	175	1.31	0.44	-0.0116 ± 0.0050	$+0.0581\pm0.0050$
					αP_Y	Y bias
B	$P<175$	154	1.16	0.38	$+0.0006\pm0.0040$	-0.0493 ± 0.0040
B	$P>175$	202	1.52	0.50	$+0.0010\pm0.0041$	-0.0447 ± 0.0041
B	All	176	1.32	0.44	$+0.0009\pm0.0029$	-0.0471 ± 0.0029
A	All	175	1.31	0.44	-0.0083 ± 0.0055	-0.0865 ± 0.0055
					αP_Z	Z bias
B	$P<175$	154	1.16	0.38	$+0.0027\pm0.0046$	-0.0883 ± 0.0046
B	$P>175$	202	1.52	0.50	$+0.0004\pm0.0043$	-0.0157 ± 0.0043
B	All	176	1.32	0.44	$+0.0020\pm0.0031$	-0.0505 ± 0.0031
A	All	175	1.31	0.44	$+0.0024\pm0.0061$	-0.0625 ± 0.0061

biases differ significantly between the two categories, the signal does not. All values of the X and Z components of the polarization are consistent with each other. The data set A shows a two-standard-deviation Y component, whereas the results for both categories of the data set B are consistent with zero.

Table V shows the data divided differently. The set B was split into high- and low-momentum samples of roughly equal amounts in order to study possible momentum-dependent effects. A similar division was not possible for the set A because of the small number of events. The same pattern is observed, the biases change substantially, the polarizations do not with the sole exception of the Y component for the set A.

A very naive calculation (without the Monte Carlo) using $(N_+ - N_-)/(N_+ + N_-)$ bin by bin in the histograms of Figs. 25 and 27 yielded results consistent with the final, more sophisticated analysis.

C. Effect of backgrounds

The EMC was used to study possible systematic errors due to backgrounds. The Ξ^- background was the largest known type, and it might induce a spurious polarization signal in two ways: by the existence of real Ξ^- polarization[38] and by a change in the beam distribution of Ξ^-'s which changes the effective acceptance of the detector for them. At most, these effects could change the Σ^- polarization by 0.000 14. This is discussed more fully in Appendix 4 of Ref. 34.

The K^- background was much smaller and can have no polarization. Its effects were negligible.

Background from straight tracks erroneously identified as kinked tracks would appear as a peak at the center of the $\cos\theta_X$ distribution, where it cannot contribute to any asymmetry. No evidence for such a peak is seen in Fig. 25. In the $\cos\theta_Z$ distribution, it would appear as a peak near $\cos\theta_Z = +1.0$. There is a slight rise in the highest bin of Fig. 27, but it is well represented by the IMC calculation for Σ^- events. Any small background from straight tracks would contribute to the bias, but not to the polarization, since it does not reverse with production angle.

The worst of these effects is far smaller than the statistical uncertainties of the Σ^- polarization. No correction was made.

D. Magnitude of the Σ^- polarization

The X and Z components of the polarizations in Table V were combined to determine the magnitude of the polarization vector given in Table VI.

E. Precession and the Σ^- magnetic moment

For a Σ^- moving through a magnetic field perpendicular to its velocity, the precession angle is given by[39]

TABLE VI. Production polarization.

Data set	Momentum bin (GeV/c)	$\langle P \rangle$ (GeV/c)	$\langle P_t \rangle$ (GeV/c)	$\langle X_F \rangle$	$\lvert \alpha\vec{P} \rvert$	$\lvert \vec{P} \rvert$
B	$P<175$	154	1.16	0.38	0.0096 ± 0.0037	0.141 ± 0.054
B	$P>175$	202	1.52	0.50	0.0112 ± 0.0040	0.165 ± 0.059
B	All	176	1.32	0.44	0.0102 ± 0.0028	0.150 ± 0.041
A	All	175	1.31	0.44	0.0118 ± 0.0053	0.174 ± 0.078
Combined		176	1.32	0.44	0.0105 ± 0.0024	0.155 ± 0.036

$$\phi=(e/\beta M_\Sigma c^2)(g/2-1)\int B\,dL$$
$$=(2/\beta\hbar c)(e\hbar/2M_\Sigma c)(g/2-1)\int B\,dL$$
$$=(g/2-1)(14.35\ \mathrm{deg/Tm})\int B\,dL\ , \tag{4.5}$$

wher $e\hbar/2M_\Sigma c$ is the Σ^- Bohr magneton, $\beta=1.000$, g is the usual g factor, and, for this experiment,

$$\int B\,dL=5.95\pm0.01\ \mathrm{T\,m}$$

is the field integral of $M2$ from the center of the production target through the downstream fringe field.

The precession angle given by Eq. (4.5) measures the change in the direction of the spin vector relative to the direction of the momentum vector. The target and detector coordinate systems used in this report were each chosen to have its Z axis along the Σ^- momentum vector in the appropriate region. Since the polarization vector at the production target is along the X axis, the precession angle is given by the direction of the final polarization vector relative to the X axis in the downstream coordinate system.

It is customary to express baryon magnetic moments in units of the proton Bohr magneton $\mu_N=(e\hbar/2M_pc)$, where M_p is the proton mass. This can be related to g by

$$\mu(\Sigma^-)/\mu_N=-(g/2)(M_p/M_\Sigma)\ . \tag{4.6}$$

The components of the final polarization are given in Table V. The initial polarization must be along the X axis, but it can be either positive or negative, giving rise to a twofold ambiguity. Further, the polarization vector could precess either clockwise or anticlockwise in the magnetic field relative to the momentum vector, another twofold ambiguity. Finally, the angle is measured modulo 360°, giving an infinite number of solutions. The full set of solutions for the precession angle ϕ can be expressed as

$$\phi=(11^\circ\pm15^\circ)+N\times180^\circ\ , \tag{4.7}$$

where $N=0,\pm1,\pm2,\ldots$. This experiment by itself cannot determine N, but when combined with other experiments only the $N=0$ solution is acceptable. Both

$$N=0\quad[\mu(\Sigma^-)=(-0.89\pm0.14)\mu_N]$$

and

$$N=-1\quad[\mu(\Sigma^-)=(+0.77\pm0.14)\mu_N]$$

are compatible with the published values obtained from fine-structure splitting.[30,31] The new result reported in Ref. 32 favors the $N=0$ value, however. In addition, a Σ^- precession experiment similar to this one, reported in Ref. 33, measured the angle ϕ for field integrals of 17.5 and 20.8 T m, compared to 5.95 T m used here. The angle ϕ for widely differing values of $\int B\,dL$ resolves the ambiguity regarding the sign of the polarization, and clearly favors the choice $N=0$.[40] Hence, the quoted value for the magnetic moment is

$$\mu(\Sigma^-)=(-0.89\pm0.14)\mu_N \tag{4.8}$$

which corresponds to a production polarization along $+X$, i.e., along the direction $+\hat{k}_{\mathrm{in}}x\hat{k}_{\mathrm{out}}$.

F. Systematic errors

This experiment measures the vector $\alpha\vec{\mathbf{P}}$, and the magnetic moment is computed directly from its direction. Therefore, the uncertainty in $\alpha=-0.068\pm0.008$ does not contribute any uncertainty to the magnetic moment. This uncertainty does affect the polarization, but it has not been included in the quoted uncertainty, since any future refinements in the value of α can be applied to the results quoted in Sec. V.

The value of the field integral is known to an accuracy of about 0.2%. This affects the magnetic moment, but not the length of the polarization vector. It is negligible in comparison with statistical uncertainties.

A number of conventional tests were made on the data to search for systematic errors. These included dividing the data sample into parts for comparison and variation of cuts. They are discussed at length in Ref. 34. The magnetic moment varied by substantially less than one standard deviation for all such tests. They included the following.

(1) Comparison of the data-set A and B results.

(2) Results for high- and low-momentum samples (Table V).

(3) Variation of the geometric and kinematic χ^2 cuts.

(4) Introduction and variation of a cut on NC pulse height.

(5) Variation of the cuts on decay-vertex position.

Another test was made to see if the analysis programs could correctly measure the known polarization of a real data sample. The data tapes were originally written in pairs at each production angle, two at +7.5 mrad followed by two at −7.5 mrad, after which the sequence was repeated. An analysis was performed by collecting the first tape from each pair into one group and the second tape from each pair into another group, and then treating the two groups as if they came from opposite production angles. The polarization resulting from such an analysis must be zero because the net polarization in each of the groups is zero. The results are $\alpha P_x=0.0010\pm0.0026$, $\alpha P_y=0.0010\pm0.0029$, and $\alpha P_z=0.0016\pm0.0032$, consistent with zero to 0.5 standard deviations.

The above test cannot reveal the presence of an error arising from a property of the beam which changes in a manner correlated with production angle. In principle, the IMC should handle such changes correctly. A successful example is the change in the vertical distribution of the beam which was discussed earlier. Nevertheless, it is useful to estimate the magnitude of such effects. Several other distributions were studied to evaluate possible systematic errors arising from production-angle-dependent differences. The technique is first discussed in terms of the Σ^- momentum distribution, and results are given for similar analyses of the χ^2 and decay-vertex distributions.

The Σ^- momentum distributions for +7.5 and −7.5 mrad are shown in Fig. 13. For this analysis, the two distributions were arbitrarily split at 175 GeV/c into high- and low-momentum sets. The number of events and the raw asymmetries of Eq. (4.4) are shown in Table VII. In order to quantify the differences in momentum distributions, we define

$$F=(N_>-N_<)/(N_>+N_<)\ ,$$

TABLE VII. Number of events and asymmetries for production-angle and momentum bins.

Production angle (mrad)	$P<175$ (GeV/c)	$P>175$ GeV/c
$+7.5$	$N=112\,660$ $A_X=-0.0263\pm0.0048$ $A_Y=-0.0487\pm0.0056$ $A_Z=-0.0856\pm0.0064$	$N=101\,540$ $A_X=-0.0270\pm0.0053$ $A_Y=-0.0437\pm0.0057$ $A_Z=-0.0153\pm0.0059$
-7.5	$N=105\,450$ $A_X=-0.0079\pm0.0049$ $A_Y=-0.0498\pm0.0058$ $A_Z=-0.0910\pm0.0066$	$N=88\,150$ $A_X=-0.0047\pm0.0056$ $A_Y=-0.0457\pm0.0061$ $A_Z=-0.0161\pm0.0063$

where $N_>$ ($N_<$) is the number of events in the bin with $P>175$ GeV/c ($P<175$ GeV/c). F is not necessarily zero, since 175 GeV/c is an arbitrary choice for the boundary. However, if the distributions for ±7.5 mrad are identical, then F_+ and F_- will be equal. We define an imbalance in the distributions

$$I=(F_+-F_-)/2\ .$$

The value of I for the momentum distribution of the full data sample is $+0.0187$.

Each $+7.5$ mrad set can be compared with each -7.5 mrad set to give four ways of computing the polarization vector P. The comparisons within the same momentum bin ($I=0.0$) are those mentioned as item 2 earlier in this section and given in Table V. "Crossover" comparisons of a high-momentum bin at one angle with a low-momentum bin at the opposite angle ($I=\pm1.0$) measure the effect of changing the momentum distribution when the production angle is reversed.

Table VIII gives the results of the polarization analysis for the crossover comparisons. For the X and Y components, the $I=\pm1.0$ analyses differ little from each other or from the full data set. The possible systematic error in these components due to this effect is estimated to be less than 0.0001. The results for the Z component differ substantially, and reverse sign with I. This is due to the momentum dependence of the bias [B_Z in Eq. (4.4)]. If we assume the effect to be linear in I, and scale to the observed value of $I=0.0187$ for the full data set, the size of the possible systematic error is 0.0007, or less than one-fourth the statistical uncertainty.

A similar analysis was performed which divided the decay-vertex distribution (Fig. 16) into two bins at $Z=650$ cm. For all three components of the polarization, the estimated systematic error was less than 0.0001.

Finally, the same analysis was done for the kinematic χ^2 distribution (Fig. 17), with the boundary at $\chi^2=0.45$. The possible systematic effects were for αP_X, $+0.0005$; for αP_Y, $+0.0002$; and for αP_Z, -0.0001. These are all small compared to the statistical uncertainties.

The most significant systematic error uncovered in this analysis is in αP_Z resulting from a slight difference in the momentum distribution for the opposite production angles. Its magnitude is one-fourth the statistical uncertainty. Since most of the polarization is in the X direction, this affects the direction, but not the magnitude. Therefore, we quote a systematic uncertainty for the magnetic moment, but not the magnitude of the polarization.

V. SUMMARY AND DISCUSSION

A. Polarization

The final result for the polarization of Σ^- produced by 400-GeV protons on beryllium is

$$P(\Sigma^-)=+0.155\pm0.036\ , \tag{5.1}$$

where the mean momentum of the Σ^- in the sample was 176 GeV/c, the transverse momentum was 1.32 GeV/c, and Feynman x was 0.44. This result assumes that $\alpha(\Sigma^-)=-0.068\pm0.008$, and the uncertainty in α is not included in Eq. (5.1). The sign quoted here was not constrained by this experiment, but was inferred by the arguments given in Sec. IV E. It means that the direction of the polarization was along $\hat{k}_{\text{in}}\times\hat{k}_{\text{out}}$. This is the same direction as Σ^+ inclusive polarization,[41] but is opposite that of Λ,[1] Ξ^0,[10] and Ξ^-.[38] (See Fig. 28.)

DeGrand and Miettinen[11] have developed a model which makes extensive predictions about the polarization of hadrons produced in a variety of inclusive reactions. One prediction of their model is that Σ^+ and Σ^- inclusively produced by protons will have polarizations with opposite sign. This is not supported by the result above.

B. Magnetic moment

The magnetic moment of the Σ^- hyperon determined in this experiment is

TABLE VIII. Polarizations computed from data sets with large momentum imbalance.

I	$+7.5$ (mrad)	-7.5 (mrad)	αP_X	αP_Y	αP_Z
$+1.0$	$P>175$	$P<175$	-0.0096 ± 0.0036	$+0.0031\pm0.0041$	$+0.0379\pm0.0044$
-1.0	$P<175$	$P>175$	-0.0108 ± 0.0037	-0.0015 ± 0.0041	-0.0348 ± 0.0045
$+0.0187$	all	all	-0.0100 ± 0.0025	$+0.0009\pm0.0029$	$+0.0020\pm0.0031$

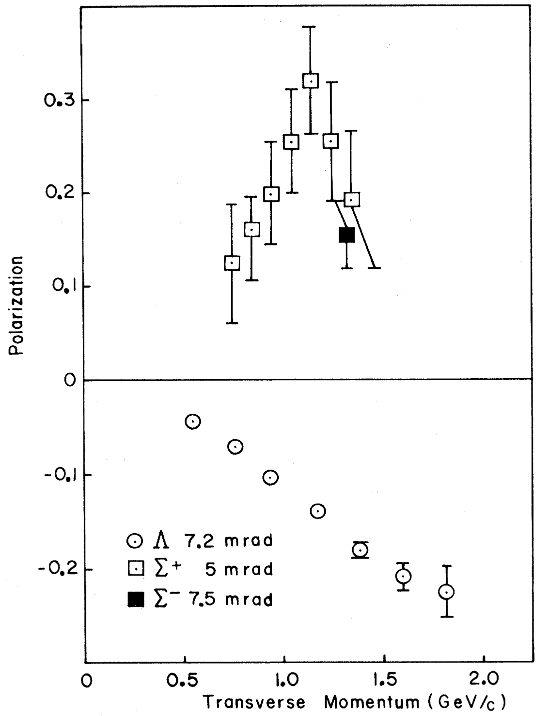

FIG. 28. A comparison of the polarization of Σ^- produced by 400-GeV protons on Be with that of Λ and Σ^+ produced under similar conditions. The data for Ξ^0 and Ξ^- are very close to those for Λ and have not been included.

$$\mu(\Sigma^-)=(-0.89\pm0.14\pm0.03)\mu_N\ , \tag{5.2}$$

where the first uncertainty is statistical, and the second is an estimate of systematic errors discussed in Sec. IV F. Other possible solutions for $\mu(\Sigma^-)$ have been rejected by the arguments given in Sec. IV E. Table IX lists all published experimental data on $\mu(\Sigma^-)$ along with the weighted average. The preliminary results from Refs. 32 and 33 are not included.

Figure 29 shows a comparison between the available experimental data and the predictions of the naive quark model which assumes that the baryon octet has an *s*-wave, color-singlet structure. The overall agreement is qualitatively quite good. Figure 30 emphasizes the differences between the simple model and the data. They are substantial, of order 0.2 nuclear magnetons, in comparison with experimental uncertainties. Various refinements to the simple model have been able to improve the agreement for individual baryons, but no fully satisfactory description of baryon magnetic moments has yet emerged.

TABLE IX. Measurements of the Σ^- magnetic moment.

Magnetic moment (nuclear magnetons)	Reference
-1.48 ± 0.37	30
$-1.40^{+0.41}_{-0.28}$	31
-0.71 ± 1.25	29
-0.89 ± 0.14	This experiment
Weighted average	
-1.00 ± 0.12	$\chi^2=3.3$ (3 DF)

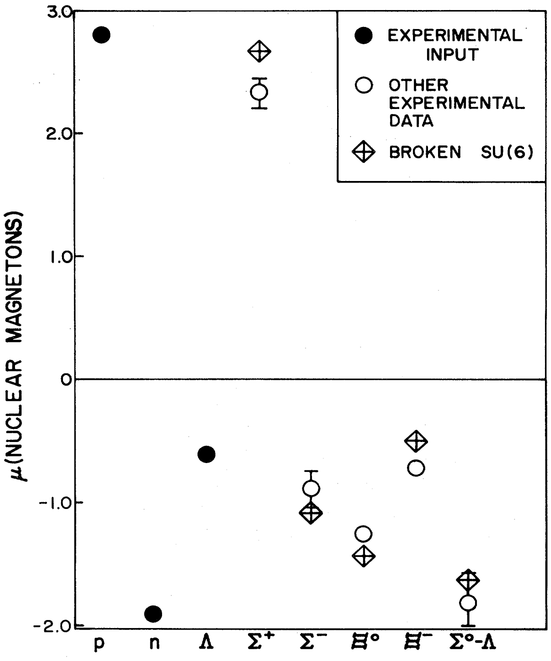

FIG. 29. A comparison of the experimental data for the magnetic moments of the baryon octet and the predictions of the naive quark model. The proton, neutron, and Λ moments have been used to compute the moments of the *u*, *d*, and *s* quarks. These, in turn, have been used to compute the moments of the other baryons. Also included is the Σ^0-Λ transition moment, an off-diagonal element of the baryon-magnetic-moment matrix. The sign of the transition moment is not known experimentally. It has been assumed to agree with theory. This graph emphasizes the qualitative agreement between experiment and theory.

ACKNOWLEDGMENTS

We wish to thank the staff of Fermilab, and particularly the staff of the Meson Laboratory for their support of this experiment. We also thank G. Ott, J. Jaske, and E. Behr for their fine technical support in building and maintaining much of the detection equipment. We are grateful to R. Thun for lending us the drift chambers. This work was supported in part by the Department of Energy and the National Science Foundation.

APPENDIX A: EXTERNAL MONTE CARLO PROGRAM

The external Monte Carlo program was written to simulate the response of our apparatus to the production and decay of Σ^- hyperons and to various types of background events. It had the following properties.

(1) The production spectrum could be either a δ function at a single chosen momentum or the spectrum experimentally determined from the data. In the latter case, the EMC spectrum at the target was adjusted to make the spectrum at the beam-channel exit fit that observed in the

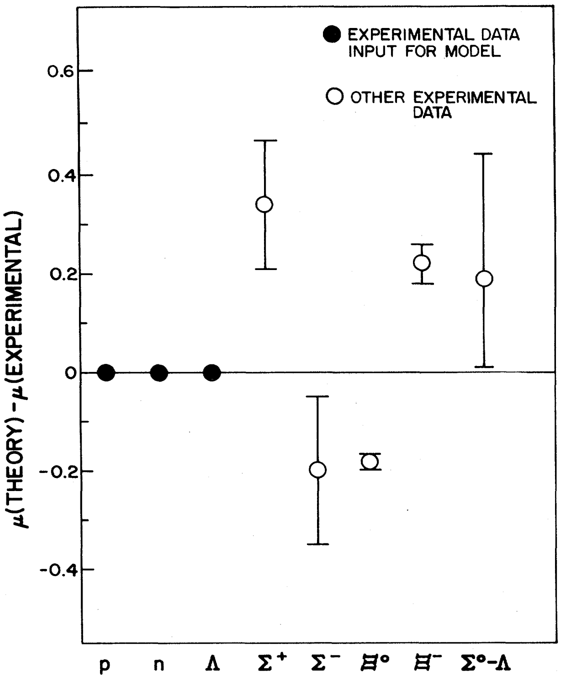

FIG. 30. A plot of the difference between the experimental and theoretical values of the magnetic moments plotted in Fig. 29. Here, the disagreement between the naive theory and experiment is emphasized. More refined models (Refs. 13—27) have made some improvements in this, but none is completely satisfactory.

real data.

(2) The target position, apertures, and trajectories through the beam channel in $M2$ were reproduced according to design and survey values and cross checked against data from straight tracks.

(3) Decay in flight of the Σ^- along its full trajectory from the production target through $C5$ position.

(4) All known properties of the spectrometer were as in the actual experiment. This included positions, apertures, resolution, inefficiencies for each wire-chamber plane, and the properties of the magnetic field up to sextupole aberrations.

(5) The daughter pions were allowed to decay.

(6) Polarization in any direction could be imposed on the Σ^- decay distribution in order to study the sensitivity of the programs to small asymmetries.

(7) A number of types of beam particles and decay products or reaction products could be propagated through the system. These included

$$\Sigma^- \rightarrow n\pi^- ,$$

$$\Xi^- \rightarrow \Lambda\pi^- , \text{ followed by} \Lambda \rightarrow n\pi^0 ,$$

$$K^- \rightarrow \pi^-\pi^0 ,$$

$$\pi^- \rightarrow \mu^-\nu^- ,$$

$$\pi^- N \rightarrow \pi^- N ,$$

negative tracks with no interaction.

APPENDIX B: INTERNAL MONTE CARLO PROGRAM

The Σ^- polarization analysis was done by evaluating the asymmetry in the angular distribution of the daughter neutron in the rest frame of the parent Σ^- with respect to each of the three spatial axes. This involved a least-squares fit of the data to the function

$$F(\cos\theta) = A(p,\pm)(1 \pm \alpha P \cos\theta) ,$$

where $A(p,\pm)$ represents the acceptance of the apparatus as a function of momentum and production angle ± 7.5 mrad. The overall acceptance of the apparatus is, in principle, independent of the production angle. However, the beam samples slightly different parts of the apparatus for the two angles. Hence, the effective acceptance function can change with angle.

In order to generate a sample of Monte Carlo events in which the parent Σ^- beam had the same characteristics as the real data, a hybrid or internal Monte Carlo (IMC) technique was used.[36] For each real event which passed all the cuts, a Monte Carlo event was generated in which the decay vertex, the production target position, and the momentum vector of the Σ^- were the same as the real event. The IMC event was generated with a random value of the angle between the neutron momentum and the X axis ($\cos\theta$ evenly distributed in the interval -1.0 to $+1.0$). The corresponding azimuthal angle was taken from the real event. This was done in the Σ^- rest system, and with a set of coordinate axes parallel to the laboratory axes. The trajectory of the resulting IMC event was then propagated through the remainder of the system and subjected to all cuts, including the straight-track χ^2 test. This procedure was repeated until ten events passed all cuts. It was then repeated again to acquire ten events each for the Y and Z axes, a total of 30 accepted IMC events.

Thus, the IMC distributions had the acceptance function of the apparatus and analysis programs folded in. All the variables that had nothing to do with the polarization analysis, the spectator variables, were taken from the real event, e.g., the Σ^- momentum, position, and direction at the decay vertex, and the azimuthal decay angle with respect to the asymmetry axis.

Histograms of both the real and IMC data were formed as functions of $\cos\theta$ (20 bins) for each of the three axes. The IMC distributions were then "polarized" with the factor $(1 + \alpha P \cos\theta)$, and αP was adjusted for minimum χ^2 in the fit of IMC data to real data.

Two complications occur in the above approach. First, some way must be found to "polarize" the IMC distributions after the acceptance function is found. This means that an analytic function which describes the shape of the $\cos\theta$ distribution as a function of polarization and acceptance is needed. Second, the polarization of the real data sample has an effect on the IMC sample, and, hence, on the acceptance determined from it. The acceptance calculation depends on the values of the spectator variables and these values are, on the average, slightly different in a polarized sample than in an unpolarized one. A solution to both problems is to attach to each real event a weight W which is proportional to its occurrence probability for a specific polarization. Thus, the effect of the real event polarization is removed by dividing the weight for each IMC event by the occurrence probability for the real event. To this end we define for each IMC event a weight

$$W=(1+\alpha P_{\mathrm{MC}}\cos\theta_{\mathrm{MC}})/(1+\alpha P_r\cos\theta_r)\ ,$$

where the denominator divides out the effect of the real polarization and the numerator polarizes the IMC distribution. The weight for an ensemble of events is the product of the weights for the individual events. Since $\alpha P_{\mathrm{MC}}=\alpha P_r$ after the fit, the weight was expanded in terms of αP:

$$W=1+\sum_i(-\alpha P)^i(\cos\theta_r)^{i-1}(\cos\theta_r-\cos\theta_{\mathrm{MC}})$$

and the first four terms were kept. This results in an analytic function with the shape of the Monte Carlo $\cos\theta$ distribution as a function of polarization parameter. Conventional χ^2 minimization techniques were used to fit it to the corresponding distribution for the real data.

---

[*] Present address: Max Planck Institute for Physics and Astrophysics, Föhringer Ring 6, D-8 München-40, Federal Republic of Germany.

[†] Present address: Fermilab, P.O. Box 500, Batavia, Illinois 60510.

[‡] Persent address: W. W. Gaertner Research, Inc., 30 Buxton Farm Rd., Stamford, Connecticut 06905.

[§] Present address: CERN, CH-1211, Geneva 23, Switzerland.

[1] G. Bunce *et al.*, Phys. Rev. Lett. 36, 1113 (1976).

[2] K. Raychaudhuri *et al.*, Phys. Lett. 90B, 319 (1980).

[3] K. Heller *et al.*, Phys. Lett. 68B, 480 (1977).

[4] F. Lomanno *et al.*, Phys. Rev. Lett. 43, 1905 (1979).

[5] S. Erhan *et al.*, Phys. Lett. 82B, 1325 (1979).

[6] K. Heller *et al.*, Phys. Rev. Lett. 41, 607 (1978); 45, 1043(E) (1980).

[7] R. Grobel, Ph.D. thesis, University of Wisconsin, 1980 (unpublished).

[8] L. Schachinger *et al.*, Phys. Rev. Lett. 41, 1348 (1978).

[9] G. Bunce *et al.*, Phys. Lett. 86B, 386 (1979).

[10] P. T. Cox *et al.*, Phys. Rev. Lett. 46, 877 (1981).

[11] T. A. DeGrand and H. I. Miettinen, Phys. Rev. D 24, 2419 (1981).

[12] B. Andersson *et al.*, Phys. Lett. 85B, 417 (1979).

[13] A useful summary of the models for magnetic moments has been made by J. Rosner, in *High Energy Physics—1980,* proceedings of the XXth International Conference, Madison, Wisconsin, edited by L. Durand and L. G. Pondrom (AIP, New York, 1981).

[14] G. E. Brown, M. Rho, and V. Vento, Phys. Lett. 97B, 423 (1980).

[15] S. Théberge and A. W. Thomas, Phys. Rev. D 25, 284 (1982).

[16] J. O. Eeg and H. Pilkuhn, Z. Phys. A 287, 407 (1978).

[17] R. G. Sachs, Phys. Rev. D 23, 1148 (1981).

[18] R. B. Teese, Phys. Rev. D 24, 1413 (1981).

[19] M. A. B. Bég, B. W. Lee, and A. Pais, Phys. Rev. Lett. 13, 514 (1964).

[20] A. De Rújula, H. Georgi, and S. L. Glashow, Phys. Rev. D 12, 147 (1975).

[21] D. A. Geffen and W. Wilson, Phys. Rev. Lett. 44, 370 (1980).

[22] N. Isgur and G. Karl, Phys. Rev. D 21, 3175 (1980).

[23] M. Bohm, R. Huerta, and A. Zepeda, Paper No. 819, XXth International Conference on High Energy Physics, Madison, Wisconsin, 1980 (unpublished).

[24] R. Verma, Phys. Rev. D 22, 1156 (1980).

[25] S. Oneda *et al.*, Paper No. 772, XXth International Conference on High Energy Physics, Madison, Wisconsin, 1980 (unpublished).

[26] Y. Tomozawa, Phys. Rev. D 19, 1626 (1979).

[27] H. J. Lipkin, Phys. Lett. 89B, 358 (1980).

[28] J. Franklin, Phys. Rev. 182, 1607 (1969); Phys. Rev. D 20, 1742 (1979).

[29] T. Hansl *et al.*, Nucl. Phys. B132, 45 (1978).

[30] B. L. Roberts *et al.*, Phys. Rev. D 12, 1232 (1975).

[31] G. Dugan *et al.*, Nucl. Phys. A254, 396 (1975).

[32] B. L. Roberts, in *High Energy Spin Physics—1982,* proceedings of the 5th International Symposium, Brookhaven National Laboratory, edited by G. Bunce (AIP, New York, 1983).

[33] J. Marriner, in *High Energy Spin Physics—1982* (Ref. 32).

[34] Leslie L. Deck, Ph.D. thesis, Rutgers University Report No. RU-81-61, 1981 (unpublished).

[35] R. Thun *et al.*, Nucl. Instrum. Methods 138, 437 (1976).

[36] G. Bunce, Nucl. Instrum. Methods 172, 553 (1980).

[37] R. Bangerter, Ph.D. thesis, University of California, 1969 (unpublished); D. Bogert *et al.*, Phys. Rev. D 2, 6 (1970); Particle Data Group, Rev. Mod. Phys. 52, S100 (1980).

[38] Regina A. Rameika, Ph.D. thesis, Rutgers University, Report No. RU-81-64, 1981 (unpublished).

[39] See, for example, V. Bargmann, L. Michel, and V. L. Telegdi, Phys. Rev. Lett. 2, 433 (1959).

[40] L. G. Pondrom, in *High Energy Spin Physics—1982* (Ref. 32).

[41] C. Wilkinson *et al.*, Phys. Rev. Lett. 46, 803 (1981).